A&A 396, 1003–1010 (2002)
DOI: 10.1051/0004-6361:20021111

Astronomy & Astrophysics

Dynamics of the solar granulation

VIII. Time and space development

A. Nesis, R. Hammer, M. Roth, and H. Schleicher

Kiepenheuer-Institut für Sonnenphysik, Schöneckstr. 6, 79104 Freiburg, Germany

Received 3 April 2002 / Accepted 30 July 2002

Abstract. We study the evolution of the granulation dynamics from the observational point of view. Based on series of excellent spectrograms taken at the VTT, Observatorio del Teide (Tenerife), in 1999, we calculated *temporal – spatial maps* of the Doppler velocity, line width, and intensity in order to track the dynamical behavior of these observables at different positions along the spectrograph slit. The Doppler velocity map reveals a granular dynamical time – the characteristic time associated with the decay of the Doppler velocity – of approximately 2 min, while the line width map does not show any characteristic time scale but rather a strong intermittence. The intensity map reveals the life time of the granulation as it is given in the literature. The granular dynamical time is practically equal to the value determined from spectrograms taken at the solar minimum 1994; so the dynamical time does not show any change over the solar cycle. The stochastic properties of the Doppler velocity and intensity data samples are studied (i) by means of their statistical moments and (ii) theoretically using presupposed model distributions. For the latter we estimated the distributions' parameters by means of the maximum likelihood method. The histograms of the Doppler velocity variations point to an asymmetric model distribution, while the histograms of the intensity variations infer a symmetric one. The intensity variations can be described well by a Gaussian probability density function, while the Doppler velocity variations are described by the double exponential (Gumbel) distribution, an asymmetric probability function. A remarkable result of the statistical analysis based on both series of observations in 1994 and 1999 is the unambiguous lack of flows with large velocity amplitudes within the intergranular space.

Key words. Sun: photosphere – Sun: granulation

1. Introduction

The empirical investigation of the evolution of the granulation dynamics can provide substantial insight into the physics of the granulation and thus into the energy transfer in the upper convective layers.

So far, our knowledge about the evolution of granulation is based mostly on studies of the emergence, splitting or merging, and disappearance of the granular intensity structures. The time scale associated with this stochastic process is the mean granular *life time* (cf. Mehltretter 1978).

Durrant & Nesis (1982) and Nesis et al. (1994) used one dimensional spatial observations (spectrograms) to examine how the granular velocity and intensity fluctuations are distributed around an average value. They found a nonsymmetrical behavior of the distributions of both observables. Krieg et al. (2000) recently showed granular intensity and velocity distributions obtained by two-dimensional observations; both distributions are again nonsymmetric. It is worthwhile to mention here that the intensity and velocity distributions in the most sophisticated numerical simulations of the granulation (cf. Asplund et al. 2000; Stein & Nordlund 2001) show a symmetrical behavior.

The temporal behavior of the granular dynamics can be investigated by series of high quality spectrograms. Due to fluctuating seeing conditions, however, it is enormously difficult to extend such investigations into the time domain.

Observational evidence for a distinct time scale that characterizes the temporal behavior of the granular dynamics has been provided for the first time by Nesis et al. (2001); elaborating a spectrogram series of 12 min they found that the change of the granular velocity patterns within the granular life time is controlled by a *dynamical time*. In 1999, we were fortunate to obtain time series of granulation spectra of consistently high quality without using a correlation tracker, with a spatial resolution of 0.3 arcsec and over periods of 20 min, sufficient for studying the time variation of characteristic granular observables at different positions along the spectrograph slit.

In the present investigation we use these observations to address (i) the temporal evolution of granular observables and their inherent time scales and (ii) the symmetry properties of the distributions of these granular observables.

Send offprint requests to: A. Nesis,
e-mail: nesis@kis.uni-freiburg.de

We assert that the history of the various positions on the solar surface gives insight into underlying stochastic processes, which control the dynamics of the granulation. We expect to find a manifestation of these processes in the temporal-spatial maps of the granular intensity, Doppler velocity, and line broadening. They allow us to study the dynamical behavior of these observables at different positions along the spectrograph slit and, furthermore, to determine the time scale characterizing each of the granular observables.

We suggest that the investigation of the symmetry properties of the distributions of granular observables may reveal the underlying random dynamical processes. We demonstrate this using histograms of velocity measurements in conjunction with theoretical probability functions. The latter are elaborated from the corresponding observations using the maximum likelihood method and correspond to Gaussian as well as non-Gaussian distributions.

We like to notice that nonsymmetric distributions infer the existence of extreme velocity or intensity values, which point to an intermittent energy transfer.

2. Material and methods

2.1. Material

The current investigation is based on series of high spatial resolution spectrograms taken during periods of exceptional seeing conditions in May 1994 and August 1999 with the German Vacuum Tower Telescope (VTT) at the Observatorio del Teide (Tenerife).

The observational material of May 1994 consists of a series of long-slit photographic spectrograms taken every 15 s at a fixed position near the center of the solar disk, covering about 20 min in total. The exposure time was 4 s and the wavelength range was $\lambda\lambda$: 491.00–491.40 nm. In this work we picked out and elaborated the spectrogram 94.A48, the best example of the series. For more details see Nesis et al. (1997, 1999).

In August 1999 further series of spectrograms were taken, again at a fixed position near the center of the solar disk every 15 s, covering about 20 min in total. The associated slit jaw images define well the position of the spectrograph slit on the solar disk (see Fig. 1). The spectrograms were recorded by an electronic Xedar imaging camera, a 2048×2048 pixel CCD system operated in frame selection mode, with an exposure time of 600 ms. We did not use a correlation tracker.

By binning 2×2 pixels we obtained a spatial scale of 0.13 arcsec per pixel and a spectral scale of 1.4 mÅ per pixel. The quality of the spectra was judged both visually, on the basis of the crispness of line wiggles at large magnification, and numerically, based on the properties of power spectra. In Fig. 1 we present the spectrogram 99S4.Sp66, which turned out to be of particularly high quality. It exhibits an rms intensity contrast of $\approx$7%. The wavelength range was again $\lambda\lambda$: 491.00–491.40 nm and included several absorption lines of different strength.

2.2. Method

From these spectrograms we obtained the fluctuations of three characteristic observables: Doppler velocity v, line broadening $FWHM$, and continuum intensity I at equidistant positions s_i along the spectrograph slit s. The velocity v represents the Doppler shift of the line core with respect to the core of the mean line profile, while $FWHM$ (full line width at half maximum) is the line broadening (cf. Nesis et al. 1993).

To prove the temperature insensitivity of the absorption lines, we calculated the line profiles by means of models with different temperatures in the solar photosphere. We verified that the lines have only a small temperature sensitivity, as expected for neutral metal lines of ca. 4 eV excitation energy. Because, furthermore, the absorption lines are to first order magnetically insensitive, the $FWHM$ reflects an unresolved photospheric velocity field w, which may well include photospheric turbulent velocity fluctuations. Thus in the following we will refer to w as line width (broadening) in velocity units as opposed to the granular convective velocity v. In this paper we make no attempt to filter out wave motions.

2.2.1. Temporal-spatial maps

Using the observed spectrogram series we investigated the *time evolution* of the granular dynamics at different positions s_i along the spectrograph slit. To do that (i) we determined the granular variables v, w, and I for each spectrogram of the series and (ii) we plotted the consecutive sets of the measurements on the time axis. The temporal behavior of the traces of v, w and I reveal the lifetimes of these characteristic observables, as well as the mergence or splitting of the corresponding granules with time.

2.2.2. Statistical analysis

It is obvious that with our spatially and temporally limited sets of the v, w, and I measurements we do not have the complete population of the granular variables (v, w, and I), but have instead a *sample*, which is a subset of the total population. On the other hand it is the central problem of physical statistics to estimate the properties of the population from the properties of a sample. In other words, based on the given observations of v, w, and I we require some knowledge about the parent population, especially about the generating mechanism by which it is produced. This, in general, is the problem of *statistical inference*.

Histograms, skewness, and kurtosis. When summarizing large amounts of raw data, we often distribute the data into classes or categories and determine the number of measurements belonging to each class. A histogram is a graphical representation of such a distribution.

To characterize the sets of measurements we used the arithmetic mean μ_a, the dispersion or scatter of the measurements within the sample characterized by the *variance* σ^2, and the skewness and kurtosis, denoted by β_1 and β_2, respectively.

Statistical inference. Of all possible methods of parameter estimation the maximum likelihood method is the most general and is widely used in practice. This method is based on the intuitive notion that the point estimate $\hat{\theta}$ of an unknown parameter θ should be chosen so that the likelihood $L(\theta)$ of a given sample $\boldsymbol{x}$ is maximized, i.e. the slope of the function is zero (see Bury 1999):

$$\left.\frac{\partial L(\theta)}{\partial \theta}\right|_{\hat{\theta}} = 0, \tag{1}$$

or equivalently,

$$\left.\frac{\partial \ln L(\theta)}{\partial \theta}\right|_{\hat{\theta}} = 0. \tag{2}$$

The maximum likelihood method has the disadvantage that in order to estimate a parameter the form of the distribution (the model) must be known.

Appropriate model distributions for the velocity v and intensity I population are suggested by their histograms. While the intensity can be described reasonably well by a symmetrical model like the Gauss distribution, the velocity requires a non-symmetric distribution like the double exponential (Gumbel) distribution. The latter is often used in astronomy to explain larger than usual observations.

The cumulative density function of the double exponential (Gumbel) distribution is

$$F(x;\,\mu,\,\sigma) = \exp\left\{-\exp\left\{-\frac{x-\mu}{\sigma}\right\}\right\}; \tag{3}$$

$$\sigma > 0,\ -\infty < x, \mu < \infty,$$

and its probability distribution function (PDF) is

$$f(x;\,\mu,\,\sigma) = \frac{1}{\sigma}\exp\left\{-\frac{x-\mu}{\sigma} - \exp\left\{-\frac{x-\mu}{\sigma}\right\}\right\}; \tag{4}$$

$$\sigma > 0,\ -\infty < x < \infty.$$

The likelihood function L of a sample of n independent observations of a Gumbel variable x is

$$L(\mu,\,\sigma) = \sigma^{-n}\ \exp\left\{-\sum_{i=1}^{n}\frac{x_i-\mu}{\sigma} - \sum_{i=1}^{n}\exp\left\{-\frac{x_i-\mu}{\sigma}\right\}\right\}. \tag{5}$$

The maximum likelihood equations (see Eq. (2)) are

$$\sum_{i=1}^{n}\exp\left\{-\frac{x_i-\hat{\mu}}{\hat{\sigma}}\right\} = n \tag{6}$$

for the maximum of L with respect to its dependence on μ, and

$$\hat{\sigma}+\hat{\mu}+\frac{1}{n}\sum_{i=1}^{n}x_i\,\exp\left\{-\frac{x_i-\hat{\mu}}{\hat{\sigma}}\right\} - \frac{\hat{\mu}}{n}\sum_{i=1}^{n}\exp\left\{-\frac{x_i-\hat{\mu}}{\hat{\sigma}}\right\} = \overline{x} \tag{7}$$

for the dependency on σ, respectively; where $\overline{x}$ is the sample average (whereas μ_a is the arithmetic set average). Substituting the first equation into the second gives an equation in $\hat{\sigma}$ only:

$$\hat{\sigma} - \overline{x} + \frac{\sum_{i=1}^{n} x_i\,\exp\left\{-\frac{-x_i}{\hat{\sigma}}\right\}}{\sum_{i=1}^{n}\exp\left\{\frac{-x_i}{\hat{\sigma}}\right\}} = 0. \tag{8}$$

The solution value $\hat{\sigma}$ is readily obtained with an equation solver. The maximum likelihood estimate $\hat{\mu}$ is then computed from (6) as

$$\hat{\mu} = -\hat{\sigma}\ln\left(\frac{1}{n}\sum_{i=1}^{n}\exp\left\{s - \frac{-x_i}{\hat{\sigma}}\right\}\right). \tag{9}$$

To examine the asymmetrical behavior of the velocity distributions we used the maximum likelihood method described above. Here, we calculated the theoretical probability density function of our measurements, and then we compared these distributions with the histograms of the measurements. This method is more reliable than a simple least-square fit of the histograms.

3. Results

Figure 1 shows the vicinity of the line Ni I 491.2 nm from an example of our series of spectrograms (namely, spectrogram 99S4.Sp66 taken in 1999). It compares the slit-jaw picture, the corresponding spectrogram, and the derived Doppler velocity and line width variations along the spectrograph slit.

Both panels are split into three parts. In the upper part we show the slit-jaw pictures representing the actual granular *topology* cut by the spectrograph slit (dark horizontal line). Attached to it are the corresponding spectrograms. They reveal the Doppler shifts indicating the *dynamics* of the granulation. Here, in the mid part of the panels in Fig. 1 the spectrograph transformed granules into bright stripes, and the intergranular space into dark stripes. The lower part shows the Doppler velocity fluctuations v along the spectrograph slit (upper panel) and the line width w (lower panel).

The correspondence between slit-jaw and spectrograms reflects actually the tight connection between granular topology and the dynamics of the granular flow. This enables us to assign the Doppler shifts v to the associated granules, and thus to the corresponding granular flow, and to localize precisely the instances of enhanced line broadening on the solar surface.

Figure 2 displays the time-space maps of these granular observables: the convective Doppler velocity v (upper panel), the line width w (middle panel), and the intensity I (lower panel). The y-axis represents the observation time, while the x-axis gives the positions on the solar surface covered by the spectrograph slit. The three maps show the history of the granulation over the entire observation time of 20 min along the spectrograph slit. Incidentally, the previous Fig. 1 is a snapshot of the granulation taken near the 1000th second of the observation.

Table 1 shows the skewness and the kurtosis of the distributions (see Sect. 2.2.2) of the Doppler velocity along the spectrograph slit measured from lines formed at different photospheric heights within the first 200 km above the continuum ($\tau_{5000} = 1$). Furthermore are displayed some spectroscopic properties of the lines used. The *skewness* gives the deviation of the probability distribution from a symmetrical form. The *kurtosis* gives the degree of peaking or flatness of the probability distribution relative to the normal probability distribution, whose kurtosis is 0. Negative values of the kurtosis reflect a flat probability distribution, positive values a peaked one. So the

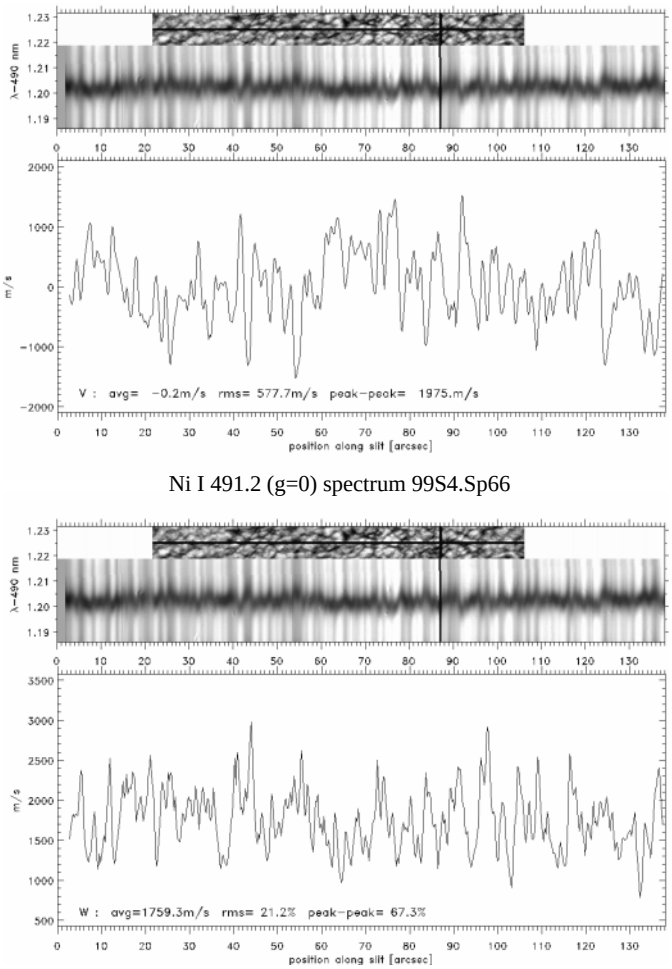

Fig. 1. Our best spectrogram (99S4.Sp66, in the wavelength region $\lambda\lambda$: 491.19–491.22 nm) with the corresponding slit-jaw white light picture attached at the top. The dark horizontal line is the spectrograph slit, while the vertical dark line is a fiducial mark. A positive Doppler velocity (upper panel) means upflows. The line width (lower panel) is expressed as a velocity.

kurtosis in Table 1 indicates flat velocity distributions with a tendency to disappear at higher photospheric layers, while the skewness points to an asymmetric Doppler velocity distribution of the deep photospheric layers. In Table 1 we realize a monotonic increase of the skewness with height in the photosphere up to nearly 200 km.

The four panels in Fig. 3 show the histograms of the Doppler velocity measurements (thin line) and overplotted (thick line, dark gray) the probability density functions (PDF) (cf. Sect. 2.2.2). The first row represents a high photospheric layer (180 km above $\tau_{5000} = 1$), the second row a deep photospheric layer (70 km above the continuum). The columns represent the PDFs of two different model distributions: the double exponential (Gumbel) distribution (left column) and the Gauss distribution (right column). A comparison of the PDFs with the associated histograms demonstrates clearly the superiority of the Gumbel distribution (first column) over the Gauss distribution (second column) to model the Doppler velocity.

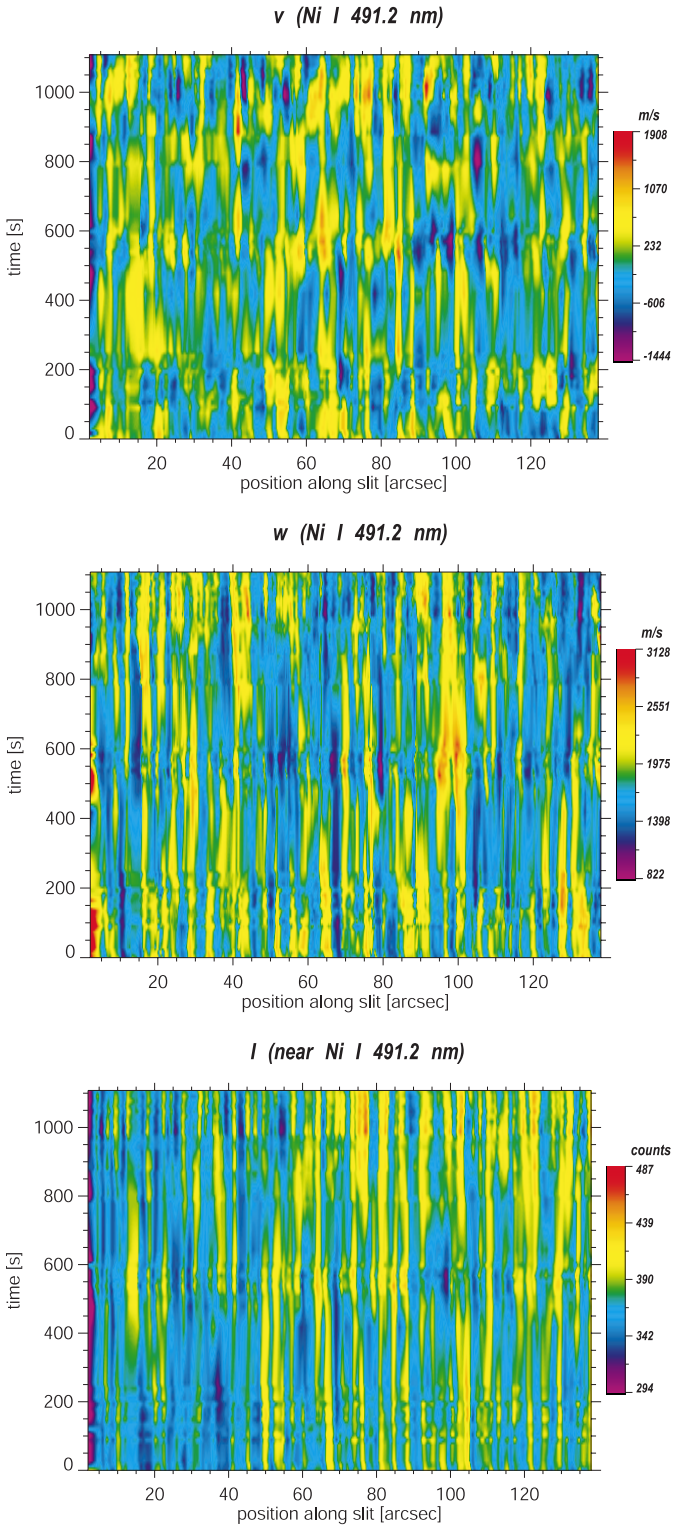

Fig. 2. Time tracking results for the granular variables convective velocity (upper panel), turbulent velocity (middle panel), and continuum intensity (lower panel).

4. Discussion

4.1. Spatial behavior of granular observables based on the best spectrogram of the series

Nesis et al. (1993) presented already nonsymmetrical velocity profiles of the granular flow and line broadening at the

Table 1. Third and fourth statistical moments of the Doppler velocity observations (May 1994 Spectrogram 94.A48) at different heights in the photosphere as well as the spectroscopic properties of the lines used.

	$\lambda\lambda^a$	$g^b_{\rm eff}$	H^c	Skewness	Kurtosis
unid.	491.31	–	70	0.29	−0.11
Fe I	491.25	1.04	100	0.39	−0.12
Fe I P	491.15	1.25	130	0.47	−0.09
Fe I	491.18	1.50	180	0.51	−0.05
Ni I	491.20	0.00	200	0.51	−0.07
Ti II	491.12	1.10	200	0.45	+0.01

[a] Wavelength in nm.
[b] Landé factor.
[c] Height in km above $\tau_{5000} = 1$.

granular borders. In the present work, Fig. 1 confirms the symmetry properties of the granular flow and the appearance of enhanced line broadening at granular borders – now, however, we are able to show these spectral properties in their context to the granular topology, so that they can be associated with individual granules, fragments, or conglomeration effects.

In Fig. 1 we find asymmetrical velocity gradients within individual granules at the position 42, which shows a well formed (pronounced) intergranular space and strong downflows; and within the large granule occupying positions 91 to 96. The latter seems to begin to fragment. Enhanced line broadening is seen at positions 41 and at position 44. Here the appearance of strong line broadening does not coincide with the maximum of the upward velocity (cf. position 43.5).

We notice also enhanced line broadening at the borders of granules with nonsymmetrical upflows – positions 73, 74, and 78 in Fig. 1. Such a behavior points to the emergence of convective rolls or bubbles on the solar surface (cf. Nesis et al. 1993).

A characteristic behavior is shown by the small granule with asymmetrical velocity profile at position 96.5 in Fig. 1. The intergranular space which surrounds this granule reveals moderate downflows, however strong line broadening at both of its borders (cf. positions 96 and 98 in Fig. 1). This observation implies that the enhanced line broadening appears preferentially at the borders of few *individual* granules within a well formed intergranular space. We will demonstrate in Sect. 4.3 that these granules emerge spontaneously from the background. Hirzberger et al. (1999), studying the evolution properties of granulation patterns, found that such spontaneous emergence of individual granules is a rare phenomenon.

It is also noteworthy that, despite the excellent quality of the spectrograms used, we never find the maximum of the line width at the position of the maximum downflow within the intergranular space; and the speed of the adjacent intergranular or granular flows is not related to the appearance of enhanced line broadening.

4.2. Temporal behavior of granular observables based on the spectrogram series

Intensity time-space map (lower panel in Fig. 2). – Bright granule structures (yellow to red color) exhibit a life time of 7–9 min, in agreement with previous results (cf. Mehltretter 1978; Hirzberger et al. 1999).

During their life time some of the granules, however, flash briefly at various locations inside their borders. De Boer et al. (1992) found small bright areas within granules especially at the border to the intergranular space. The authors interpreted this "common granular feature" as the signature of strong upflows or of shocks in supersonic convection.

Dark intergranular spaces (blue to violet color) appear most prominently in the region 0 to 50 along the spectrograph slit. Most of them can be followed over the whole observing time, while the rest is interrupted by structures of mean (green to yellow color) intensity.

In the position range 50 to 150, on the other hand, we rarely find prominent intergranular spaces (blue color); most of the time this region is governed by a mean continuum. At some places, however, short-lived intergranular regions are formed with strong downflows, as evidenced by the convective velocity map. These intergranular regions are sporadically distributed over the observing time and do not show any characteristic life time.

The slightly different behavior of the left and right part of the intensity map, and to some extent also the velocity map, could be due to large scale fluctuations of convective properties.

Remarkable is the appearance of isolated short-lived intergranular regions (blue color) in the right half of the map, opposite to the long-lived intergranular spaces in the left part of the map.

As a matter of surprise these isolated dark areas are formed during the evolution of the mean continuum (shown in green color in Fig. 2) instead of following a preceding granule. In this context these small intergranular spaces are associated with a reduction of the mean intensity, while granules are formed by an enhancement of the intensity. Two explanations are possible: either these events reflect the dynamics of granules that are not covered by the spectrograph slit, or they are the result of the collapse of granules in layers deeper than $\tau_{5000} = 1$ (see Skartlien 1998).

Doppler velocity map (upper panel in Fig. 2). – In the upper panel of Fig. 2 we follow the change of the Doppler velocity at the spectrograph slit positions with time.

What we realize immediately in this map is the short life time of the granular velocity patterns represented by the length of the yellow or red strips. The average length of these strips amounts to only 200 s. This time scale is in agreement with the dynamical time of the granular velocity structures reported by Nesis et al. (2001).

When we now follow the history of the positions simultaneously in the intensity and velocity maps, we see that there are positions on the solar surface where a granule

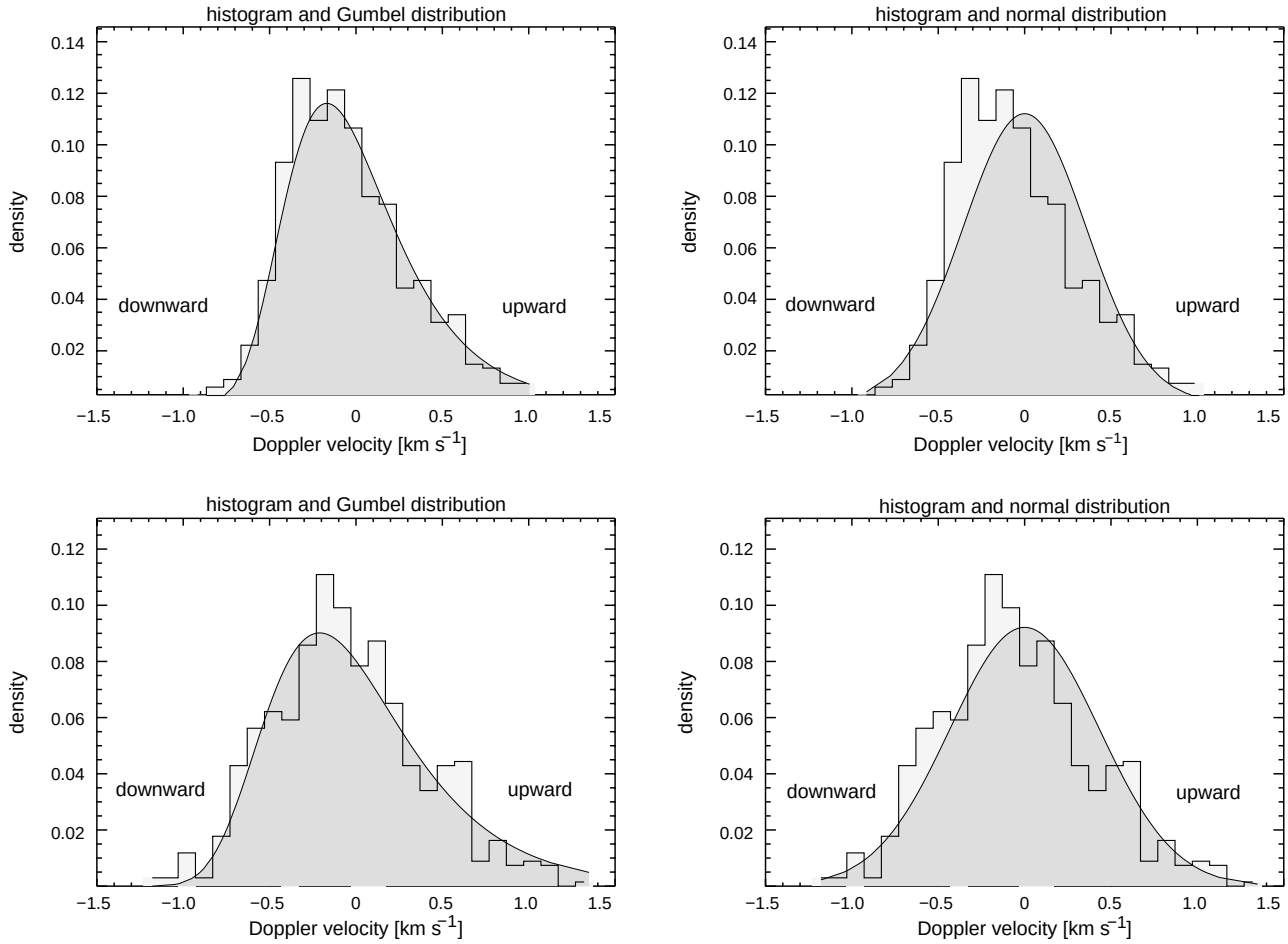

Fig. 3. Histogram and probability density function PDF of the Doppler velocity measurements (May 94 spectrogram 94.A48) at two different heights in the photosphere. *Bottom row*: 70 km; *top row*: 180 km above $\tau_{5000} = 1$.

(see intensity map) exhibits at least two relative maxima of convective upflows (see convective velocity map, e.g. position 41.5 arcsec near time 850–1000 s and position 64 arcsec, near time 540–690 s) over its life time, often with extreme velocities.

This could explain why we did not find, so far, correlation coefficients between granular intensity and velocity with values higher than 0.7 (cf. Nesis et al. 1992), as would be expected for convective energy transport. The best spectrogram of our current series, 99S4.Sp66 (cf. Fig. 1), taken at the 1000th second of the observation, shows a correlation between the velocity and intensity of the order of 0.7.

We assert that the full coincidence of maximal velocity and intensity must be a rare event in the solar granulation. Over our observing time the intensity and velocity maps display such a coincidence only in the last 150 s in the position range 70 to 85 in Fig. 2.

The emergence of a second convective upflow during the life time of a granular intensity structure could also be the reason for the appearance of bright small areas within granules, especially at the border to the intergranular space (cf. de Boer et al. 1992).

The velocity map (Fig. 2, upper panel) is certainly influenced by the presence of wave motions. They might well be responsible for a regular pattern that appears in this figure.

Line broadening map (middle panel in Fig. 2). – This map exhibits the variation with time of the line width along the spectrograph slit. Red and blue represent enhanced and reduced line broadening, respectively.

In this map the length of the red or blue paths signifies the duration of periods with enhanced or reduced line broadening.

The line broadening variations do not show a prominent mean time value characterizing the persistence of periods with enhanced or reduced line broadening on the solar surface, in contrast to the granular intensity and velocity structures. Enhanced line broadening (red strips) may persist on the solar surface for any time between 100 and 400 s.

It is obvious that the duration of enhanced or reduced line broadening reflects the relaxation time of the dynamical processes underlying the line broadening variations. Thus, in the case that the line broadening variation is due to turbulence, its diffusion time must also lie between 100 and 400 s (cf. Nesis et al. 1999).

Taken together, the maps of line broadening, Doppler velocity, and intensity in Fig. 2 show again that enhanced line broadening appears at the granular borders (see position range 0 to 50 along the slit). Important, however, is the fact that enhanced line broadening occurs always at the granular borders over the entire observing time. This finding is in agreement with our previous results (cf. Nesis et al. 1993).

On the other hand, the exclusive appearance of enhanced line broadening at granular borders implies that the underlying process might be an intrinsic property of the granulation dynamics that is not governed by a single time of relaxation. Nesis et al. (1993) suggested that the appearance of enhanced line broadening is tightly connected with shear layers at granular borders.

Nesis et al. (1999) studied the spatial variations of the line broadening along the spectrograph slit based exclusively on a single excellent spectrogram. They found only one position along the variation.

According to the line broadening map in our Fig. 2, however, a large spatial gradient of the line broadening along the spectrograph slit seems to be a frequent event on the solar surface.

As we can see in this map, at the beginning of the observation there is only one position (at positions 2 to 3) along the spectrograph slit with large spatial peak to peak variation of the line broadening (red/blue color).

Over the observing time, however, we observe that practically all the positions (for example position 44 at 1000 s) along the slit exhibit large spatial variations of the line broadening at different moments of the observation.

Another important aspect of the granulation dynamics is the time behavior of the spatial variations of the line broadening, especially in case the line broadening variation is due to turbulence. Then large spatial peak to peak variations correspond to a large ratio of turbulent to gas pressure on the solar surface. Thus according to the above results we expect to find everywhere on the solar surface occasionally large values of the ratio of turbulent to gas pressure (cf. Nesis et al. 1999).

4.3. Temporal behavior of the granular dynamics in three detailed examples

Individual granule. – At the time 920 s of the observation, a granular structure with associated convective upflow emerges at position 42. On both sides of the granule we find well formed intergranular spaces associated with downflows; strong downflows appear ≈100 s after the onset of the granular flow (see intensity and velocity maps in Fig. 2). This granular configuration extends up to the end of the observation, i.e. for about 120 s.

Of particular interest is the short duration of the appearance of the moderate intensity and velocity values emerging at the 820 s. Both observables decline in the following practically to their mean values. The enhanced line broadening, however, remains unchanged for the next 120 s; the intensity shows another two maxima at 920 s.

A snapshot taken at 1000 s during this evolution is shown in Fig. 1; in the slit-jaw image, one can clearly see the individual granule at position 42.

Isolated intergranular space. – An isolated intergranular region is formed at time 900 s and spatial position 54 (cf. Fig. 2). The appearance of the intergranular region is associated with strong convective downflows, as we can see in the velocity map (upper panel).

We notice (i) their short dynamical time, and (ii) the lack of an enhanced line broadening associated with the maximum downflow. Strongly enhanced line broadening emerges rather at the spatial position 56, as we can see in the line broadening map in Fig. 2. According to the slit-jaw images, this spatial position 56 marks the border of a tiny individual granule with small velocity (cf. Fig. 1, which corresponds to a slightly later time).

Large fragmented granule. – At time 900 s a large granular structure of moderate intensity and short life time appears at spatial positions 91–95 in Fig. 2. This large granule is associated with strong nonsymmetrical upflow and an enhanced line broadening at its border. We like to point out here the short duration of the convective flow as well as of the enhanced line broadening.

4.4. Theoretical probability density functions of the Doppler velocity measurements

Table 1 shows the statistical properties of the current Doppler velocity measurements (spectrogram 94.A48) and their variation with the height in the photosphere. The skewness and kurtosis of these measurements infers again an asymmetrical behavior of their distribution, which furthermore varies with the height in the photosphere.

A glance at the left column of Fig. 3 shows that the asymmetric Gumbel probability density function describes precisely the extreme values of the Doppler velocity measurements at the solar surface, in contrast to the normal probability density function (cf. right column of Fig. 3).

In Fig. 3 we recognize, furthermore, a small difference in the behavior of the velocity fields of the deeper and higher photospheric layers: A comparison between PDFs and histograms in the first column in Fig. 3 shows that the Gumbel distribution represents better the velocities of the higher layers (left panel, top row) than those of the deeper layers (left panel, bottom row). Here, the asymmetrical behavior of the histograms in the deeper layers is due to the contribution of the upward velocities, whereas in the higher photospheric layers the asymmetry of the distribution seems to be the result of the lack of downward velocities.

We realize, furthermore, the clearly nonsymmetrical behavior of the Doppler velocity distribution. This asymmetry implies a bias towards large granular velocities. In spite of the high spatial resolution of our observations, we do not find equally large downward velocities. The large upward velocities

raise the question about the physical process underlying the asymmetrical behavior of the velocity distribution.

5. Conclusions

The time-space maps of our observables demonstrate clearly their temporal evolution at various positions on the solar surface and reveal their characteristic time scales.

- The evolution of the intensity shows a characteristic time scale of the order of 7 min. This time gives the typical duration of enhanced intensity at any position and reflects the life time of the granular intensity structure.
- The evolution of the granular flow reveals a characteristic time scale of the order of 2 to 5 min. This time is defined by the decay of the Doppler velocity of the granular flow and thus represents a dynamical time of the granule.
  We think that the two characteristic time scales needed in describing the granular evolution address two partially different processes associated with the intensity and velocity, respectively.
- The evolution of the line width reveals a time scale of 2 to 5 min, which characterize the persistence of the enhanced line broadening (at the granular borders). In case that the line broadening is due to turbulence the persistence time is associated with the diffusion time of the turbulence into the intergranular space.
- Intergranular regions do not show any particularity in their evolution and they do not reveal a characteristic time.
  The lack of a specific evolution of the intergranular space raises the question about the nature of its dynamics. We find here enhanced line broadening but not as strong as at the granular borders. The investigation of the intergranular space is tightly connected with the spatial resolution and thus with the seeing conditions of the observations.
- The model distributions of the Doppler velocity show an asymmetry towards upward velocities.
  The existence of large upward velocities, which are now supported also by our statistical analysis, seems to be a proven fact and raises the question about the cause of these large granular velocities and thus about the source of the asymmetry of the distribution.

We assert that the time-space maps of our observables as well as their model distributions confirm previous results on the granular dynamics and present new aspects of photospheric dynamics.

Acknowledgements. We are grateful to the referee, Dr. J. A. Bonet, for his thoughtful comments on the manuscript.

References

Asplund, M., Ludwig, H.-G., Nordlund, Å., & Stein, R. F. 2000, A&A, 359, 669
de Boer, C. R., Kneer, F., & Nesis, A. 1992, A&A, 257, L4
Bury, K. 1999, Statistical Distributions in Engineering (Cambridge Univ. Press)
Durrant, J. C., & Nesis, A. 1982, A&A, 111, 272
Hirzberger, J., Bonet, J. A., Vázquez, M., & Hanslmeier, A. 1999, ApJ, 515, 441
Krieg, J., Kneer, F., Koschinsky, M., & Ritter, C. 2000, A&A, 360, 1157
Mehltretter, J. P. 1978, A&A, 62, 311
Nesis, A., Hanslmeier, A., Hammer, R., et al. 1992, A&A, 253, 561
Nesis, A., Hanslmeier, A., Hammer, R., et al. 1993, A&A, 279, 599
Nesis, A., Hammer, R., & Hanslmeier, A. 1994, in Cool Stars, Stellar Systems, and the Sun, ed. J.-P. Caillault, PASPC, 64, 655
Nesis, A., Hammer, R., Hanslmeier, A., et al. 1997, A&A, 326, 851
Nesis, A., Hammer, R., Kiefer, H., et al. 1999, A&A, 345, 265
Nesis, A., Hammer, R., Roth, M., & Schleicher, H. 2001, Sol. Phys., 200, 11
Skartlien, R. 1998, Ph.D. Thesis, Univ. Oslo
Stein, R. F., & Nordlund, Å. 2001, in Helioseismic Diagnostics of Solar Convection and Activity, ed. T. L. Duvall, Jr., J. W. Harvey, A. G. Kosovichev, & Z. Švestka (Kluwer Academic Publishers), 91